

# Imaging Laser-Induced Choroidal Neovascularization in the Rodent Retina Using Optical Coherence Tomography Angiography

Jang Ryul Park,<sup>1</sup> WooJhon Choi,<sup>1,2</sup> Hye Kyoung Hong,<sup>3</sup> Yongjoo Kim,<sup>1</sup> Sang Jun Park,<sup>3</sup> Yoonha Hwang,<sup>4</sup> Pilhan Kim,<sup>4</sup> SeJoon Woo,<sup>3</sup> Kyu Hyung Park,<sup>3</sup> and Wang-Yuhl Oh<sup>1</sup>

<sup>1</sup>Department of Mechanical Engineering, Korea Advanced Institute of Science and Technology (KAIST), Daejeon, Republic of Korea

<sup>2</sup>Information and Electronics Research Institute, Korea Advanced Institute of Science and Technology (KAIST), Daejeon, Republic of Korea

<sup>3</sup>Department of Ophthalmology, Seoul National University College of Medicine, Seoul National University Bundang Hospital (SNUBH), Bundang-gu, Seongnam, Gyeonggi-do, Republic of Korea

<sup>4</sup>Graduate School of Nanoscience and Technology, Korea Advanced Institute of Science and Technology (KAIST), Daejeon, Republic of Korea

Correspondence: Kyu Hyung Park, Department of Ophthalmology, Seoul National University College of Medicine, Seoul National University Bundang Hospital (SNUBH), 173-82 Gumi-ro, Bundang-gu, Seongnam, Gyeonggi-do 13620, Republic of Korea; jiani4@snu.ac.kr

Wang-Yuhl Oh, Department of Mechanical Engineering, Korea Advanced Institute of Science and Technology (KAIST), 291 Daehak-ro, Yuseong-gu, Daejeon 34141, Republic of Korea; woh1@kaist.ac.kr

JRP, WC, and HKH contributed equally to this work.

Submitted: December 15, 2015

Accepted: March 11, 2016

Citation: Park JR, Choi W, Hong HK, et al. Imaging laser-induced choroidal neovascularization in the rodent retina using optical coherence tomography angiography. *Invest Ophthalmol Vis Sci.* 2016;57:OCT331–OCT340. DOI:10.1167/iovs.15-18946

**PURPOSE.** The purpose of this study was to evaluate the performance of optical coherence tomography angiography (OCTA) in visualizing laser-induced choroidal neovascularization (CNV) in the rodent retina.

**METHODS.** Choroidal neovascularization was induced via laser photocoagulation in 2 male Brown Norway rats and 2 male C57BL/6 mice. For qualitative comparison, the animals were imaged in vivo with OCTA, indocyanine green angiography (ICGA), and fluorescein angiography (FA), and ex vivo with immunofluorescence confocal microscopy, 14 days post laser photocoagulation without anti-vascular endothelial growth factor (anti-VEGF) intervention. For longitudinal quantitative analysis, CNV was induced in 6 additional male C57BL/6 mice. Three mice intravitreally received an anti-VEGF agent and the remaining 3 mice phosphate buffered saline (PBS) vehicle 7 days post laser photocoagulation. These animals were imaged using OCTA 6, 14, and 21 days post laser photocoagulation. The area and volume of the laser-induced CNV lesions were measured longitudinally.

**RESULTS.** In both mice and rats, OCTA qualitatively showed high correlation with FA, ICGA, and immunofluorescence imaging. Unlike FA and ICGA, which does not show the microvasculature due to dye leakage, OCTA visualized the CNV microvasculature with resolution and contrast comparable to immunofluorescence images. Longitudinal imaging enabled normalization of the CNV area and volume, reducing inherent variation in the CNV size. By using only 3 mice in each group, statistically significant differences ( $P < 0.01$ ) in the CNV area and volume could be demonstrated.

**CONCLUSIONS.** Optical coherence tomography angiography enables noninvasive visualization of the laser-induced CNV microvasculature in the rodent retina with high resolution and tissue-lumen contrast, providing quantifiable in vivo measurements for longitudinal analysis.

**Keywords:** optical coherence tomography, angiography, choroidal neovascularization, rodent

Choroidal neovascularization (CNV) is characteristic of exudative age-related macular degeneration (AMD), one of the leading causes of irreversible vision loss and blindness. Choroidal neovascularization is characterized by the growth of abnormal vessels from the choroid penetrating through Bruch's membrane and extending into the subretinal pigment epithelium (sub-RPE) or subretinal space, which results in degeneration of the sub-RPE and photoreceptor.<sup>1-3</sup>

Utilizing small animals is essential for understanding pathophysiology and pharmaceutical development because of the constraints of using the human retina. Many rodent models of ocular diseases have been developed and utilized for retinal disease research due to their ease of maintenance and availability.<sup>4-12</sup> In particular, laser-induced CNV in the rodent retina is a popular model for AMD research. In this model, laser

photocoagulation is performed to injure Bruch's membrane, which stimulates the growth of abnormal blood vessels from the choroid into the subretinal space.<sup>8-11</sup> Unlike in management of AMD in human patients, where the presence and location of CNV are difficult to know, the precise location of the laser-induced CNV lesion in the rodent retina is known prior to imaging. Therefore, imaging of laser-induced CNV in animal models has more emphasis on assessing the progress of the lesion than on detecting its presence, which makes noninvasive and high-resolution angiographic imaging techniques highly desirable for this application.

Widely used imaging techniques for laser-induced CNV include fluorescein angiography (FA), indocyanine green angiography (ICGA), and choroidal flat mount immunofluorescence imaging. Fluorescein angiography and ICGA are



representative imaging modalities for monitoring CNV in vivo.<sup>13-17</sup> In FA images, the presence of CNV manifests as diffuse hyperfluorescence due to fluorescein dye leakage. Therefore, although highly effective in detecting the presence of CNV, FA does not well visualize the detailed structure of CNV vessels. Indocyanine green angiography suffers less from obscuring of the CNV vessel structure than does fluorescein because of the higher chemical affinity of indocyanine green to the plasma protein albumin, which has a significantly larger molecular size than fluorescein and indocyanine green.<sup>13</sup> However, both FA and ICGA are not capable of providing depth-resolved images of blood vessels in the retina and choroid. Minor disadvantages of FA and ICGA include relatively short imaging time windows following intravenous injection of the dye. Finally, choroidal flat mount imaging precludes longitudinal monitoring of individual animals, although it provides contrast and resolution better than commonly used in vivo imaging techniques.

Optical coherence tomography (OCT) is a noninvasive imaging technique that allows cross-sectional imaging of biological tissue. Optical coherence tomography angiography (OCTA), a functional extension of OCT, combined with ultrahigh imaging speeds, can visualize not only the retinal structure but also vasculature in three-dimensions without administration of exogenous contrast agents. Optical coherence tomography angiography derives its contrast from erythrocyte movement resulting in local fluctuation of OCT intensity and/or phase, which in turn can be used to map the location of blood vessels by comparing sequentially acquired cross-sectional images from the same position on the retina.<sup>18-27</sup> Recent advances in OCT technology enabled clinical application of OCTA on imaging human patients with various retinal diseases, including AMD,<sup>28-30</sup> diabetic retinopathy,<sup>31,32</sup> and glaucoma.<sup>33</sup> In particular, it has been shown multiple times that OCTA is highly suitable for imaging CNV because it can readily distinguish normal vessels in the inner retina from abnormal vessels in the outer retina due to its high depth resolution. Optical coherence tomography angiography has also been applied on imaging the retina in a number of small animal models, including rats with elevated intraocular pressure and obese mice.<sup>34,35</sup>

In this study, we have demonstrated OCTA for imaging laser-induced choroidal neovascularization in the rodent retina. A prototype high-speed OCT system utilizing a custom ring cavity wavelength-swept laser at the center wavelength of 1048 nm with an A-scan rate of 230 kHz was developed for rodent retinal imaging. Laser-induced CNV in the mouse and rat retina were imaged to visualize the three-dimensional microvasculature. In addition to OCTA, FA, ICGA, and immunofluorescence imaging were performed in the same eyes for comparison. In the mouse retina, we demonstrated longitudinal monitoring of laser-induced CNV in two groups, one of which intravitreally received an anti-vascular endothelial growth factor (anti-VEGF) agent with known efficacy and the other phosphate buffered saline (PBS) vehicle only. By measuring the CNV area and volume longitudinally using OCTA, a statistically significant effect of the anti-VEGF was shown using relatively small numbers of animals.

## METHODS

### Animal Model

Male Brown Norway rats with body weights of 200 to 250 g and C57BL/6 male mice with body weights of 25 to 30 g were used for this investigation. All animals were housed with a

normal 12 h/12 h light/dark cycle. For all animal procedures described below, animals were anesthetized using ketamine (80 mg/kg for rats and 100 mg/kg for mice) and xylazine (8 mg/kg for rats and 10 mg/kg for mice) with appropriate additional doses as necessary to maintain anesthesia. Tropicamide (1%) was applied topically for dilation.

Laser photocoagulation was performed using an argon laser (Lumenis, Inc., Santa Clara, CA, USA) with a center wavelength of 532 nm. An incident power of 250 mW, spot size of 200  $\mu$ m, and pulse duration of 100 ms for rats and 100 mW, 100  $\mu$ m, and 100 ms for mice were used to rupture Bruch's membrane. Four to 5 lesions were induced evenly distributed around the optic nerve head (ONH) on the right eye approximately 1.4 mm and 0.7 mm away from the ONH for rats and mice, respectively. Successful injury was confirmed by formation of a bubble immediately after laser photocoagulation. Eyes showing significant subretinal hemorrhage after laser photocoagulation were excluded. Rats and mice were returned to their normal housing after recovering from anesthesia.

Seven days after laser photocoagulation, 6 mice were randomly divided into 2 groups, with 1 group intravitreally receiving an anti-VEGF agent (Aflibercept, 5 mg/mL in 1  $\mu$ L PBS vehicle; Bayer Pharma AG, Berlin, Germany) and the other 1  $\mu$ L of PBS vehicle only on the right eye ( $n = 3$  for both groups). Both the anti-VEGF and control groups underwent OCTA imaging 1 day before, 7 days after, and 14 days after intravitreal injection.

Seven and 14 days after laser photocoagulation, an additional 2 rats and 2 mice for each time point underwent FA, ICGA, OCTA, and immunofluorescence imaging of the choroidal flat mount for comparison. None of the animals here received intravitreal injection prior to imaging. The animals were anesthetized and dilated as described previously. Fluorescein angiography and ICGA were performed immediately after OCTA imaging, after which the animals were killed for choroidal flat mount preparation.

All animals were treated in accordance with the ARVO Statement for the Use of Animals in Ophthalmic and Vision Research, and animal care and treatment were performed under protocols approved by the institutional review boards at Korea Institute of Advanced Science and Technology and Seoul National University Bundang Hospital.

### OCTA Imaging

Animals were imaged using a prototype high-speed OCT system utilizing a custom ring cavity wavelength-swept laser at the center wavelength of 1048 nm with an A-scan rate of 230 kHz. Areas measuring 1.7  $\times$  1.7 mm for mice and 3.2  $\times$  3.2 mm for rats were scanned centered at the ONH. For both rats and mice, 3 B-scans each were acquired from 1024 cross-sectional locations. With a total of 3072 B-scans with 820 A-scans/B-scan, the resulting B-scan time interval and total volume acquisition time were approximately 4.45 ms and 13.7 seconds, respectively, with a scan duty cycle of 80%. From each cross-sectional location, speckle decorrelation normalized to have values between 0 and 1 was calculated between two sequentially acquired B-scans in linear intensity scale to generate cross-sectional OCT angiograms.<sup>36</sup> To separate the choroidal and retinal microvasculature, Bruch's membrane was segmented semiautomatically in ImageJ software (<http://imagej.nih.gov/ij/>; provided in the public domain by the National Institutes of Health, Bethesda, MD, USA).<sup>37</sup> The rough boundary between the outer nuclear layer and outer plexiform layer was manually segmented to separate the inner retina containing normal retinal microvasculature from the outer retina containing abnormal CNV. For two-dimensional visualization, each volumetric angiogram

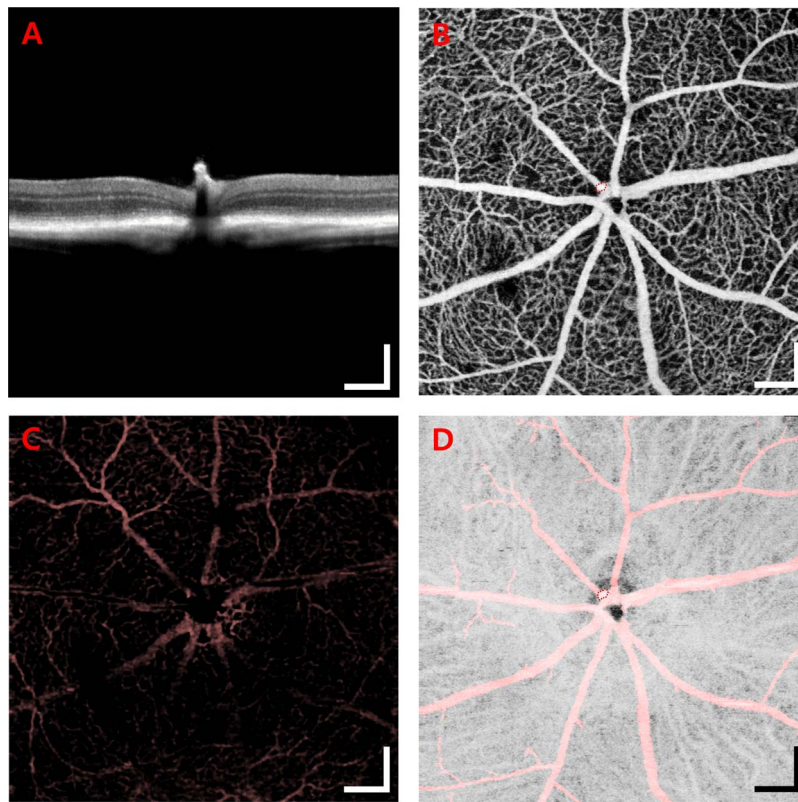


**FIGURE 1.** Optical coherence tomography angiography images of the normal mouse retina. (A) An OCT intensity cross-section at the optic nerve head, with 55 B-scans averaged to increase image quality. (B) An en face OCT angiogram of the inner retina. (C) An en face OCT angiogram of the outer retina. Shadow artifacts caused by thick retinal vessels in the inner retina are shaded in red. (D) An en face OCT angiogram of the choroid. Artifacts near the center of the images, caused by parasitic reflections from the lens in the OCT system, are delineated by the red dotted contour. Scale bars: 200  $\mu$ m.

was projected separately in three depth ranges, resulting in en face angiograms of the inner retina, outer retina, and choroid. For CNV area measurement, the vessel area was calculated by binarizing the en face angiogram of the outer retina and summing the number of pixels above the threshold. For CNV volume measurement, the vessel volume was calculated by summing the number of voxels in the binarized volumetric angiogram of the outer retina.

### FA and ICGA Imaging

Immediately after OCTA imaging, select animals were scanned using two separate confocal scanning laser ophthalmoscope (CSLO) prototypes for FA and ICGA imaging. Fluorescein sodium (10 mg for mice and 40 mg for rats intraperitoneally; Alcon, Fort Worth, TX, USA) and indocyanine green (0.375 mg for mice and 1.5 mg for rats, intravenously; Daiichi Pharmaceutical, Tokyo, Japan) were injected approximately 6 minutes prior to imaging. For both FA and ICGA,  $1.7 \times 1.7$  mm and  $3.2 \times 3.2$  mm areas centered at the ONH were scanned for rats and mice, respectively. The CSLO systems used light sources at 488 nm and 785 nm for excitation of fluorescein and indocyanine green, respectively. A high numerical aperture objective lens (PlanApo $\lambda$ , numerical aperture = 0.75; Nikon Corp., Tokyo, Japan) was used as the ocular lens. Fluorescence emission at 500 to 550 nm and 813 to 870 nm was detected by a multialkali photomultiplier tube (R9110; Hamamatsu, Shizuoka Pref., Japan). The electric signal from the photomultiplier tube was digitized by a frame grabber (Solios; Matrox Electronic Systems,

Quebec, Canada) and reconstructed to a  $512 \times 512$ -pixel image.

### Choroidal Flat Mount Preparation for Immunofluorescence Imaging

Immediately after *in vivo* imaging, select animals were intracardially perfused with PBS 14 days post laser photocoagulation. After PBS perfusion, eyes were enucleated. Within 4 hours after enucleation, the eyes were fixed in 2% paraformaldehyde/PBS for 30 minutes for rats and 10 minutes for mice. The choroid was isolated and permeabilized with 0.5% Triton X-100, 5% fetal bovine serum, 5% normal goat serum, and 20% DMSO in PBS for 3 hours at room temperature. The mouse choroid was incubated in a 1  $\mu$ g/mL hamster anti-mouse CD31 (EDM Millipore Corp., Temecula, CA, USA) solution at 4°C for 2 days. After washing, the choroid was incubated for 4 hours at room temperature in a secondary antibody solution with 1:300 dilution of goat anti-Armenian hamster IgG (Alexa Fluor488 AffiniPure; Jackson ImmunoResearch Laboratories, Inc., West Grove, PA, USA). The rat choroid was incubated in a 10  $\mu$ g/mL lectin-BS-1-FITC (Sigma-Aldrich Corp., St. Louis, MO, USA) solution at 4°C for 2 days. Four cuts were made from the edges to the center after thoroughly washing the choroid, which was then flattened and mounted with the vitreous side up on a microscope slide. The choroidal flat mount was visualized with a confocal microscope (LSM710; Carl Zeiss, Oberkochen, Germany).

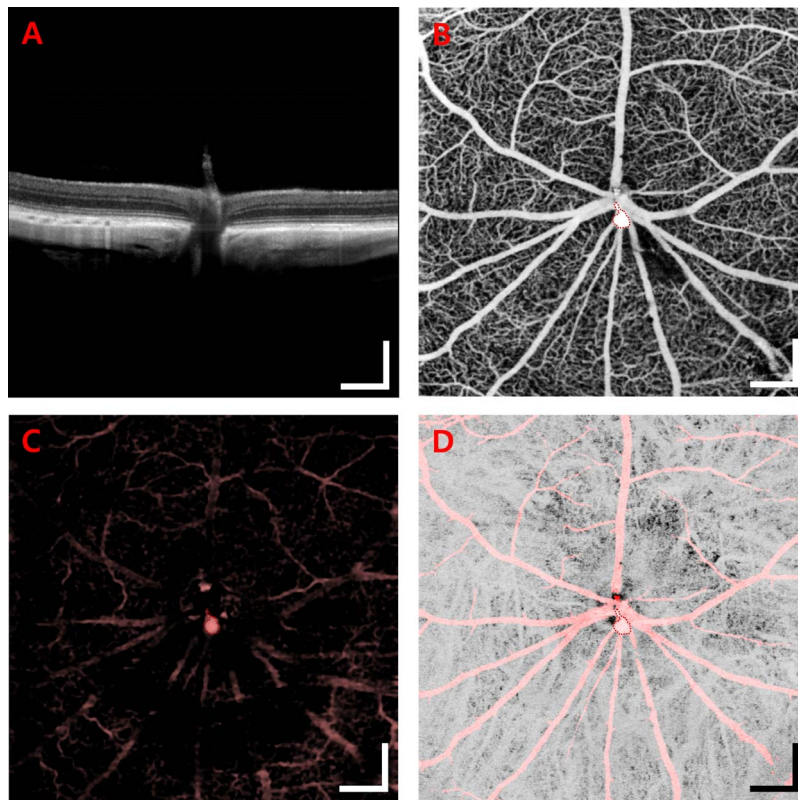


**FIGURE 2.** Optical coherence tomography angiography images of the normal rat retina. (A) An OCT intensity cross-section at the optic nerve head, with 55 B-scans averaged to increase image quality. (B) An en face OCT angiogram of the inner retina. (C) An en face OCT angiogram of the outer retina. (D) An en face OCT angiogram of the choroid. Shadow artifacts caused by thick retinal vessels in the inner retina are shaded in red. Artifacts near the center of the images, caused by parasitic reflections from the lens in the OCT system, are delineated by the red dotted contour. Scale bars: 400  $\mu\text{m}$ .

### Statistical Analysis

For CNV area and volume measurements using OCTA, means and standard deviations were calculated separately for the anti-VEGF and control groups at each time point. Multiple lesions in the same eye were not treated as statistically independent, and the mean values were used as a single measurement for statistical analysis. To test for statistical significance between the two groups, the Student's *t*-test was used with the null hypothesis rejection criterion of  $P < 0.01$ .

### OCT Prototype

The schematic of the high-speed OCT prototype is shown in Supplementary Figure S1. The ring cavity wavelength-swept laser was built using a semiconductor optical amplifier (SOA) (SOA-1060-100-HI-24dB; INNOLUME GmbH, Dortmund, Germany) and a tunable Fabry-Perot filter (TFPF) (H1050-140-700; Lambda Quest, Canoga Park, CA, USA).<sup>38,39</sup> The TFPF was driven sinusoidally at approximately 57.5 kHz using a function generator (DS345; Stanford Research Systems, Sunnyvale, CA, USA). The output of the SOA was synchronously modulated with a square wave to generate unidirectional sweeps at approximately 57.5 kHz with a duty cycle of approximately 25%. The optical output of the ring cavity was buffered 4 $\times$ , resulting in an OCT A-scan rate of approximately 230 kHz and a wavelength tuning range of approximately 94 nm centered at 1048 nm. An acousto-optic frequency shifter at 85 MHz (AMF-85-1060-ER60; Brimrose, Sparks, MD, USA) was used in the OCT reference arm to double the 6-dB sensitivity roll-off imaging range.<sup>40</sup> The OCT signal was detected using a

balanced detector (PDB460C; Thorlabs, Inc., Newton, NJ, USA) and sampled at 340 MHz using a high-speed analog-to-digital converter (PX14400; Signatec, Lockport, IL, USA). With the incident power on the retina of approximately 1.2 mW, the measured system sensitivity was 96 dB with a single-side 6-dB roll-off imaging range of approximately 1.5 mm in air. The OCT sample arm was configured using Zemax software (Zemax LLC, Seattle, WA, USA) to have a lateral resolution of approximately 22  $\mu\text{m}$ . The measured axial resolution was approximately 6.9  $\mu\text{m}$  in tissue.

### RESULTS

Figures 1A and 2A show OCT intensity B-scans at the ONH, Figures 1B and 2B en face OCT angiograms of the inner retina, Figures 1C and 2C en face OCT angiograms of the outer retina, and Figures 1D and 2D en face OCT angiograms of the choroid of the mouse and rat, respectively. The B-scan and angiograms were extracted from single volumetric scans of  $1024 \times 1024 \times 3$  A-scans over  $1.7 \times 1.7$  mm (Fig. 1) and  $3.2 \times 3.2$  mm (Fig. 2) areas centered at the ONH. In normal mice and rats, the outer retina is avascular, and any decorrelation signal in Figures 1C and 2C is due to shadows caused by thick retinal vessels in the inner retina, which can be easily identified by comparing Figures 1B and 1C and Figures 2B and 2C, respectively. Similarly, major arterioles and venules cast a shadow in Figures 1D and 2D. For unambiguous identification of shadow artifacts, areas directly under thick retinal vessels are shaded in red in Figures 1C and 1D and Figures 2C and 2D.

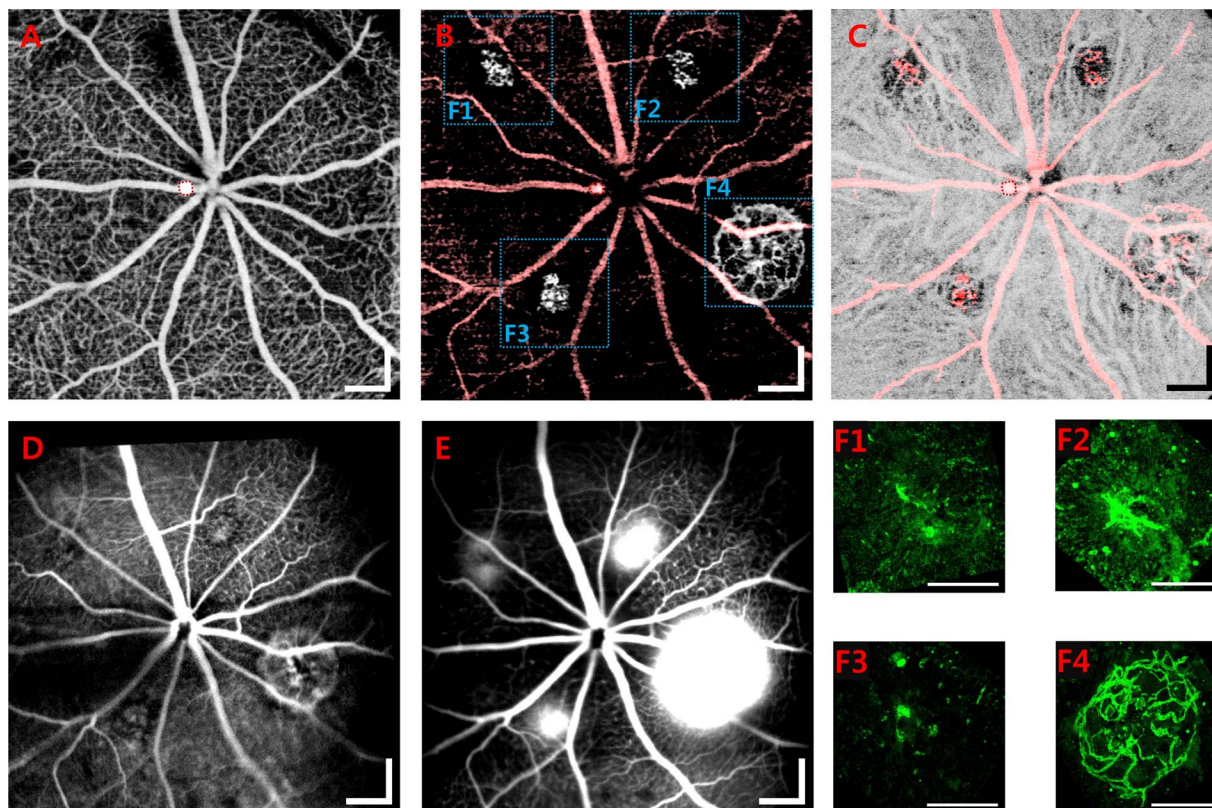


**FIGURE 3.** Optical coherence tomography angiography, ICGA, FA, and immunofluorescence images of laser-induced CNV in the mouse retina without anti-VEGF intervention. Imaging was performed 14 days after laser photocoagulation without anti-VEGF intervention. En face OCT angiograms of (A) the inner retina, (B) the outer retina, and (C) the choroid. Shadow artifacts due to retinal vessels and thick vessels from laser-induced CNV are shaded in red. Artifacts caused by parasitic reflections from the lens are delineated by the red dotted contour. (D) Indocyanine green angiography and (E) FA showing dye leakage from the CNV lesion as hyperfluorescence. (F1–F4) Immunofluorescence images of the laser-induced CNV from the CD31-stained choroidal flat mount. Immunofluorescence images were rotated to match the orientation of the CNV lesions shown in (B) for better comparison. Scale bars: 200  $\mu$ m.

To demonstrate the performance of OCTA in visualizing laser-induced CNV, OCTA, ICGA, FA, and immunofluorescence imaging were performed in the mouse and rat retina 7 and 14 days after laser photocoagulation without anti-VEGF intervention. Figures 3 and 4 acquired from the mouse and rat retina, respectively, 14 days after laser photocoagulation, show (Figs. 3A, 4A) en face OCT angiograms of the inner retina, (Figs. 3B, 4B) en face OCT angiograms of the outer retina, (Figs. 3C, 4C) en face OCT angiograms of the choroid, (Figs. 3D, 4D) ICGA, (Figs. 3E, 4E) FA, and Figure 3 (F1–F4) and Figure 4 (F1–F5) immunofluorescence images of laser-induced CNV from CD31-stained choroidal flat mounts. Note that laser-induced CNV can be well visualized in the otherwise avascular outer retinal angiogram. Shadow artifacts from the inner retina are shaded in red in Figures 3B and 4B. Note that thick vessels from laser-induced CNV in addition to retinal vessels cast shadow artifacts in Figures 3C and 4C. Compared to ICGA shown in Figures 3D and 4D, FA in Figures 3E and 4E show markedly higher degree of hyperfluorescence from CNV lesions, completely obfuscating the CNV vasculature underneath. However, despite significantly less hyperfluorescence, ICGA does not well visualize the CNV microvasculature either, due to dye leakage. Immunofluorescence images in Figures 3F and 4F show detailed CNV microvasculature, which can be compared with OCT angiograms in Figures 3B and 4B. Supplementary Figure S2 shows close-up OCTA, immunofluorescence, and ICGA images of the CNV lesion indicated as F4 in Figure 3 for better comparison. Supplementary Figures S3 and S4 show the

corresponding results from the mouse and rat retina, respectively, 7 days after laser photocoagulation.

To demonstrate longitudinal imaging of laser-induced CNV using OCTA, OCT imaging was performed 6, 14, and 21 days post laser photocoagulation with 1 group of mice receiving intravitreal injection of an anti-VEGF agent (Aflibercept) and the other group receiving the PBS vehicle 7 days post laser photocoagulation. Figures 5A and 6A show en face OCT angiograms of the inner retina, Figures 5B and 6B en face OCT angiograms of the outer retina, Figures 5C and 6C en face OCT angiograms of the choroid, and Figures 5D and 6D select cross-sectional OCT angiograms of representative mice from the control and anti-VEGF groups, respectively. Images from multiple points are shown to visualize the effect of the anti-VEGF agent on laser-induced CNV. The CNV area in the control mouse qualitatively visualized in Figures 5B1 through 5B3 do not change significantly over time. However, the CNV area in the anti-VEGF mouse in Figures 6B1 through 6B3 decreases noticeably over time. A similar trend can be seen in the representative cross-sectional OCT angiograms, Figures 5D and 6D, acquired from the same transverse location on the retina. Note that outer retinal flow corresponding to laser-induced CNV is colored in red. Figure 7, showing time series plots of the means and standard deviations of normalized CNV areas and volumes for the control and anti-VEGF groups, respectively, summarizes the effect of the anti-VEGF agent on laser-induced CNV. The effect of the anti-VEGF agent was minimal in

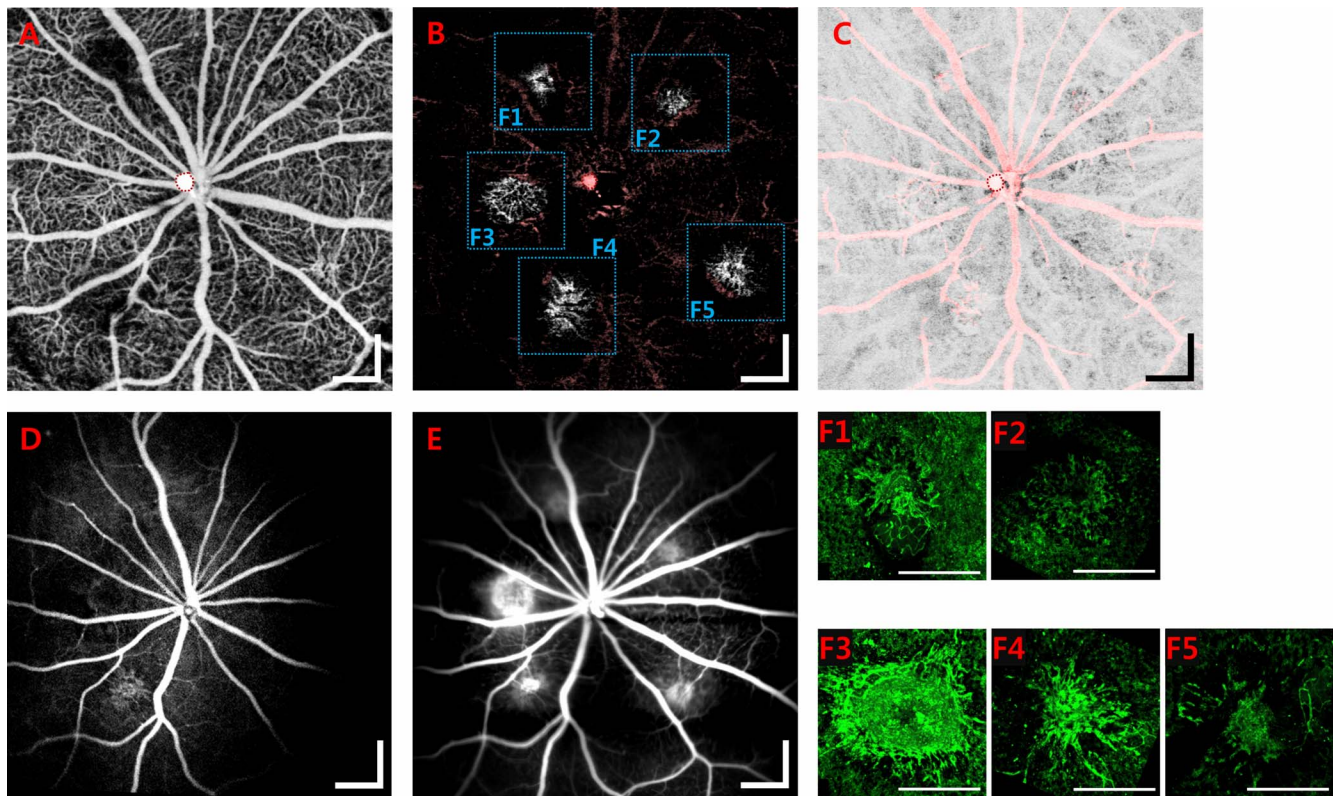


**FIGURE 4.** Optical coherence tomography angiography, ICGA, FA, and immunofluorescence images of laser-induced CNV in the rat retina without anti-VEGF intervention. Imaging was performed 14 days after laser photocoagulation without anti-VEGF intervention. En face OCT angiograms of (A) the inner retina, (B) the outer retina, and (C) the choroid. Shadow artifacts due to retinal vessels and thick vessels from laser-induced CNV are shaded in red. Artifacts caused by parasitic reflections from the lens are delineated by the red dotted contour. (D) Indocyanine green angiography and (E) FA showing dye leakage from the CNV lesion as hyperfluorescence. (F1–F5) Immunofluorescence images of the laser-induced CNV from the lectin-FITC-stained choroidal flat mount. Immunofluorescence images were rotated to match the orientation of the CNV lesions shown in (B) for better comparison. Scale bars: 400  $\mu\text{m}$ .

the choroid, as can be qualitatively visualized in Figures 5C and 6C.

## DISCUSSION

Since longitudinal imaging in animal models is highly advantageous for understanding pathogenesis and pharmaceutical development, OCT is an attractive imaging technique because of its ability to visualize cross-sections of the retina and choroid noninvasively. Multiple studies have used structural OCT in investigating laser-induced CNV in rodent models.<sup>41–43</sup> High imaging speeds enable acquisition of full volumetric scans over areas sufficiently large for visualization of laser-induced CNV in the rodent retina without significant motion artifact. Structural OCT images allow quantitative analysis of the retinal thickness and qualitative visualization of the CNV lesion. However, contrast between the lumen and surrounding tissues is usually insufficient for clear visualization of the CNV microvasculature in structural OCT images.

As shown in Figures 3 and 4, OCTA has the advantage that it noninvasively provides the detailed CNV microvasculature comparable to immunofluorescence images of the choroidal flat mount. Although immunofluorescence provides highest resolution images of the CNV microvasculature, choroidal flat mount preparation has a significant disadvantage in that it requires enucleation of the eye, which precludes longitudinal

monitoring of the same animal. Because the size and shape of the CNV microvasculature varies significantly, ex vivo techniques necessitate cross-sectional measurements in a relatively large number of animals to achieve statistical significance. In contrast, OCT allows longitudinal imaging that allows normalization of CNV areas and volumes, which can significantly reduce the number of animals required by reducing the effect of inherent variation in CNV sizes. To demonstrate this, a commercial anti-VEGF agent with known efficacy was used in this study where only 3 eyes from the control group and 3 eyes from the anti-VEGF group were sufficient to achieve statistically significant difference with  $P < 0.01$ , as shown in Figures 5 through 7.

Unlike FA and, to a lesser degree, ICGA, which clearly visualize dye leakage in the form of hyperfluorescence, immunofluorescence imaging and OCTA do not directly show leakage. In imaging patients with AMD, FA has been a useful imaging technique for diagnosing the presence of CNV because the CNV lesion clearly appears hyperfluorescent due to leakage. However, dye leakage obfuscates the detailed CNV microvasculature, which renders FA unsuitable for visualization of the microvasculature itself. Indocyanine green angiography suffers less from dye leakage because of its higher chemical affinity to larger plasma albumin molecules<sup>13</sup> but still does not well visualize the CNV microvasculature with sufficiently high resolution. Clinically, dye leakage has not been considered a serious limitation because leakage itself could be used as a

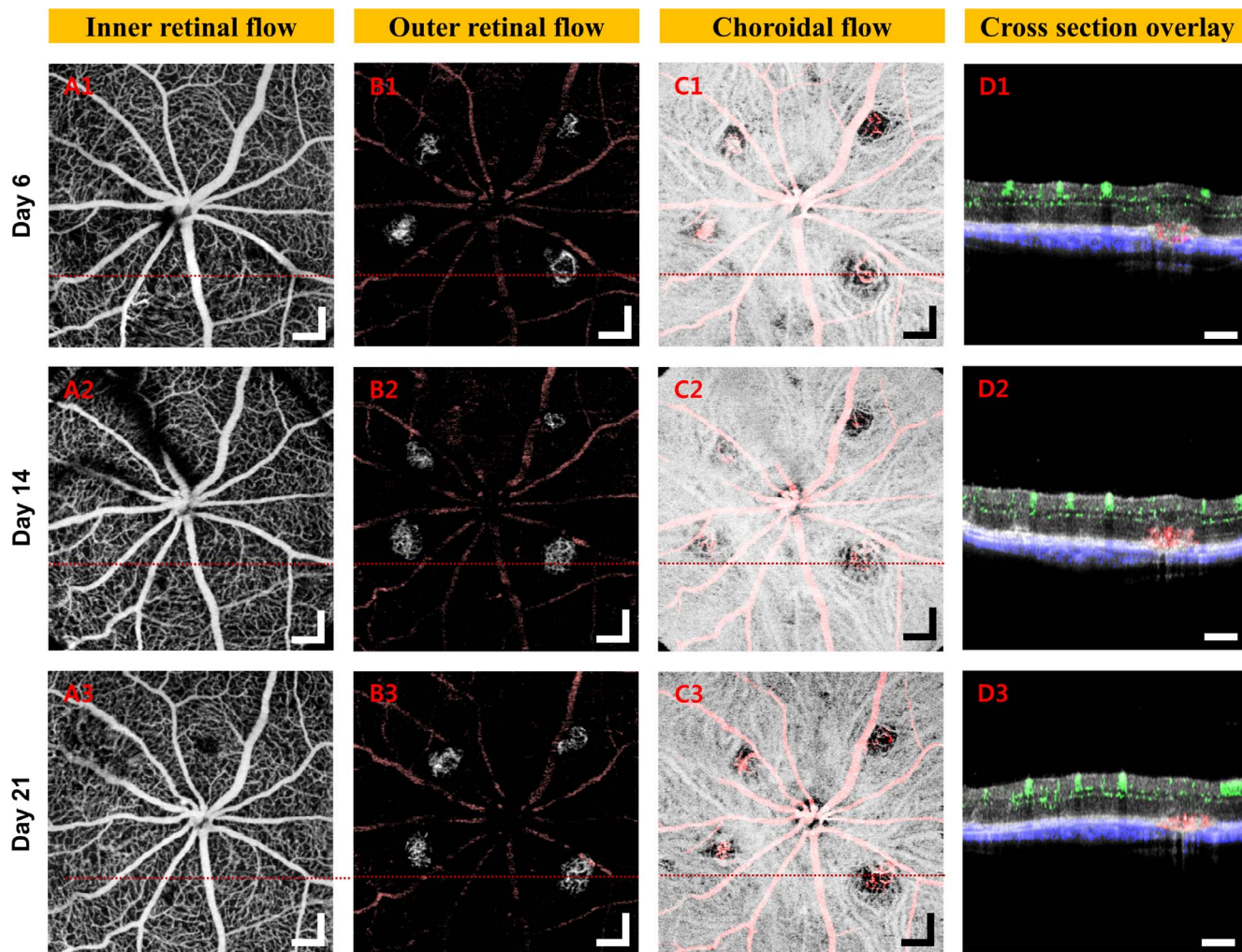


**FIGURE 5.** Longitudinal OCTA imaging of laser-induced CNV in the mouse retina receiving intravitreal injection of PBS. Imaging was performed 6, 14, and 21 days post laser photocoagulation. Intravitreal injection of the PBS vehicle was performed 7 days post laser photocoagulation. En face OCT angiograms of (A) the inner retina, (B) the outer retina, and (C) the choroid. Shadow artifacts due to retinal vessels and thick vessels from laser-induced CNV are shaded in red. (D) Select cross-sectional OCT angiograms extracted from the locations indicated by the red lines in (A–C) show inner retinal flow (green), outer retinal flow (red), and choroidal flow (blue). The outer retinal flow corresponds to laser-induced CNV. The CNV lesions do not change significantly over time. Scale bars: 200  $\mu$ m.

marker for the presence of CNV, which is initially unknown in AMD patients.

For small animal imaging, however, the ability to visualize the laser-induced CNV microvasculature may prove to be more important than the ability to detect hyperfluorescence, an indirect effect of CNV. Note that unlike CNV in patients, the presence of CNV artificially induced via laser photocoagulation is usually not the unknown in investigations using rodent models. Therefore, hyperfluorescence from CNV has limited utility if it does not provide more information than merely the presence of CNV. For understanding pathogenesis and pharmaceutical development, direct visualization of the CNV microvasculature may provide more information and make quantitative analysis easier. Because OCT is a three-dimensional imaging technique, OCTA can provide both the area and volume of abnormal CNV vessels. Furthermore, because OCTA is an extension of OCT, other structural information such as the retinal thickness can be extracted from inherently coregistered volumetric images of the retinal structure. This multifunctionality makes OCT highly advantageous in investigations using small animal models.

Because OCTA requires multiple cross-sections repeatedly acquired from the same location, higher imaging speeds are required for acquiring an OCTA volume compared to acquiring a structural OCT volume. Recent advances in OCT imaging speeds enabled commercialization of OCTA for patients, which currently shows promising applications in a wide range of ophthalmic diseases. Specifically, OCTA has been shown to visualize CNV microvasculature in patients better than FA and ICGA.<sup>28,29</sup> In this study, we evaluated the ability of OCTA in visualizing laser-induced CNV in the rodent retina. Because animals are anesthetized for OCT imaging, relatively slow imaging speeds can be tolerated for rodent OCTA. Therefore, we believe that this technique can be readily adopted in small animal investigations using commonly available OCT systems. However, note that the OCT imaging speed determines the interscan time interval, which, when excessively long, can induce significant bulk motion artifacts from eye motions, even under anesthesia.

The current investigation had a few limitations. Major arterioles and venules in the inner retina, as well as relatively thick CNV vessels, resulted in rapid attenuation of the OCT

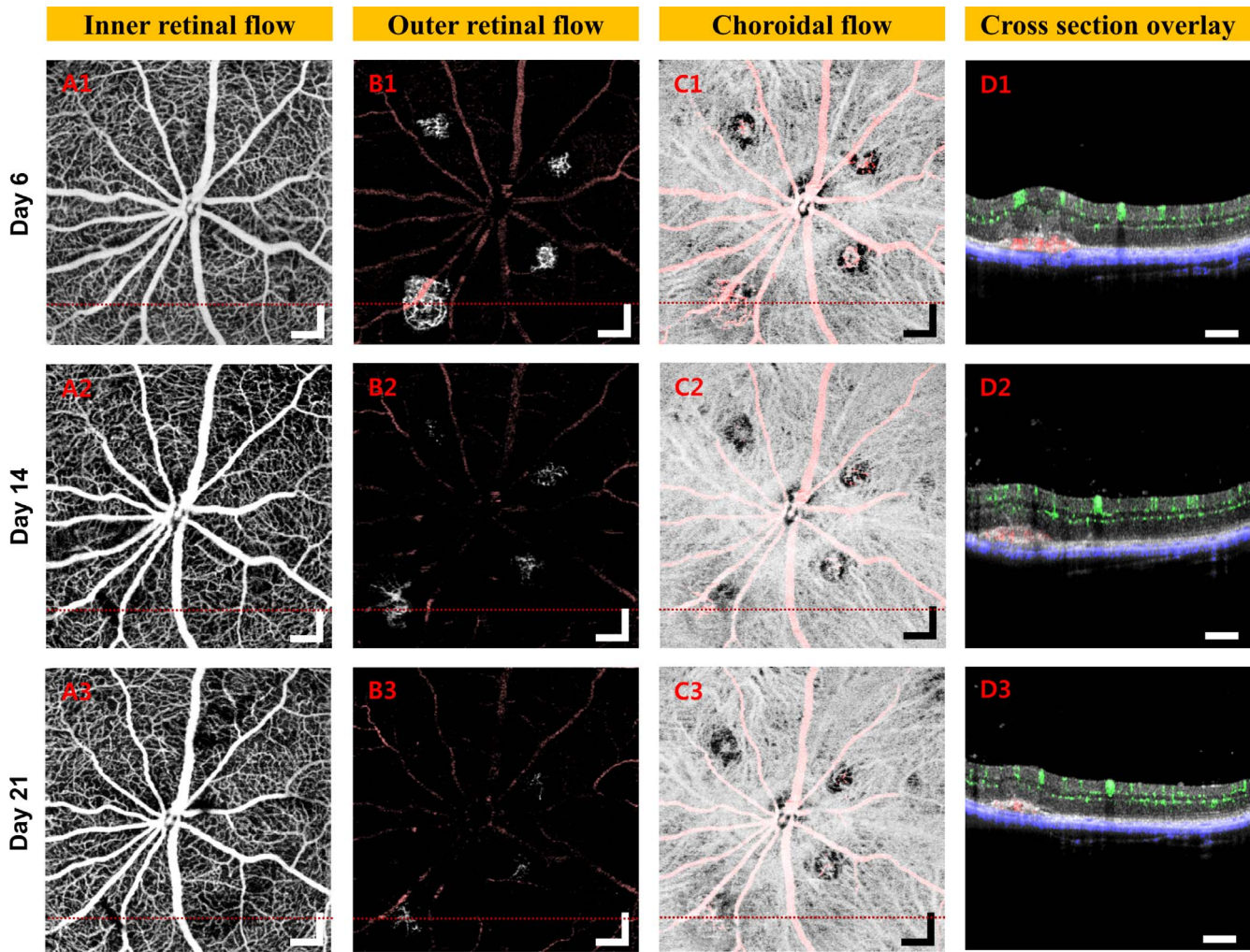


FIGURE 6. Longitudinal OCTA imaging of laser-induced CNV in the mouse retina receiving intravitreal injection of an anti-VEGF agent, Aflibercept. Imaging was performed 6, 14, and 21 days post laser photocoagulation. Intravitreal injection of Aflibercept was performed 7 days post laser photocoagulation. En face OCT angiograms of (A) the inner retina, (B) the outer retina, and (C) the choroid. Shadow artifacts due to retinal vessels and thick vessels from laser-induced CNV are shaded in red. (D) Select cross-sectional OCT angiograms extracted from the locations indicated by the red lines in (A–C) show inner retinal flow (green), outer retinal flow (red), and choroidal flow (blue). The outer retinal flow corresponds to laser-induced CNV. The CNV areas decrease over time. Scale bars: 200  $\mu$ m.

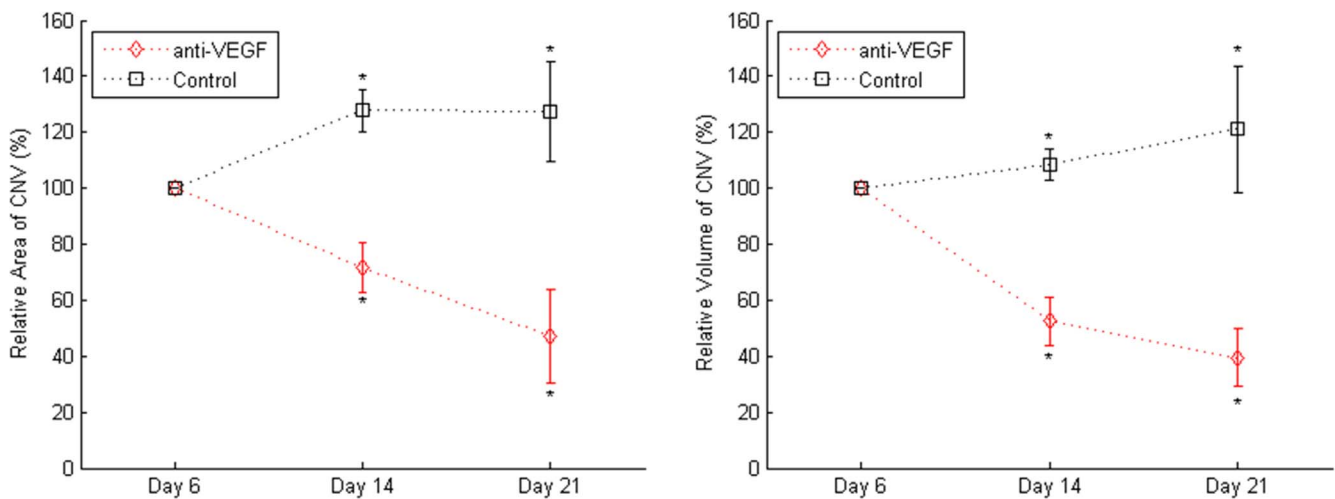


FIGURE 7. Normalized area and volume of laser-induced CNV measured using OCTA. Choroidal neovascularization areas and volumes at different time points were normalized with respect to areas and volumes measured on day 6. Multiple CNV lesions from the same eye were not treated as statistically independent, and the mean value was used as a single measurement for a given time point.  $N = 3$  for each time point. The error bar shows the standard deviation of the measurement. \*Indicates  $P < 0.01$ .

signal in depth, which resulted in spurious decorrelation signals appearing as shadow artifacts underneath the vessels. Although this limitation is mostly irrelevant for two-dimensional analyses using en face projection angiograms, it may overestimate the CNV volume if not carefully inspected. Development of postprocessing algorithms for removing shadow artifacts can be helpful. Regardless, the current investigation strongly suggests that OCTA can be a powerful in vivo imaging technique for investigations using animal models of laser-induced CNV. Other potentially helpful features include quantitative measurement of flow speeds using OCTA, which may require an imaging speed higher than what was used in this investigation to differentiate multiple flow speed ranges. Applications of OCTA on other animal models of retinal diseases are underway.

### Acknowledgments

The authors thank Jaeryung Kim at the Graduate School of Medical Science and Engineering, Korea Advanced Institute of Science and Technology, for his contribution in managing the animal model used in this investigation. This work was supported in part by the Ministry of Health & Welfare of Korea (HI15C0001), the National Research Foundation (NRF) of Korea (NRF-2013R1A1A3012306), and the End-Run Project of Korea Advanced Institute of Science and Technology (KAIST).

Disclosure: **J.R. Park**, None; **W. Choi**, None; **H.K. Hong**, None; **Y. Kim**, None; **S.J. Park**, None; **Y. Hwang**, None; **P. Kim**, None; **S.J. Woo**, None; **K.H. Park**, None; **W.-Y. Oh**, None

### References

- Ferris FL III, Fine SL, Hyman L. Age-related macular degeneration and blindness due to neovascular maculopathy. *Arch Ophthalmol*. 1984;102:1640-1642.
- Ambati J, Ambati BK, Yoo SH, Ianchulev S, Adamis AP. Age-related macular degeneration: etiology, pathogenesis, and therapeutic strategies. *Surv Ophthalmol*. 2003;48:257-293.
- Bressler NM. Age-related macular degeneration is the leading cause of blindness. *JAMA*. 2004;291:1900-1901.
- Kern TS, Engerman RL. A mouse model of diabetic retinopathy. *Arch Ophthalmol*. 1996;114:986-990.
- Robinson R, Barathi VA, Chaurasia SS, Wong TY, Kern TS. Update on animal models of diabetic retinopathy: from molecular approaches to mice and higher mammals. *Dis Model Mech*. 2012;5:444-456.
- Neufeld AH, Sawada A, Becker B. Inhibition of nitric-oxide synthase 2 by aminoguanidine provides neuroprotection of retinal ganglion cells in a rat model of chronic glaucoma. *Proc Natl Acad Sci U S A*. 1999;96:9944-9948.
- Libby RT, Smith RS, Savinova OV, et al. Modification of ocular defects in mouse developmental glaucoma models by tyrosinase. *Science*. 2003;299:1578-1581.
- Ryan SJ. The development of an experimental model of subretinal neovascularization in disciform macular degeneration. *Trans Am Ophthalmol Soc*. 1979;77:707-745.
- Dobi ET, Puliafito CA, Destro M. A new model of experimental choroidal neovascularization in the rat. *Arch Ophthalmol*. 1989;107:264-269.
- Tobe T, Ortega S, Luna JD, et al. Targeted disruption of the FGF2 gene does not prevent choroidal neovascularization in a murine model. *Am J Pathol*. 1998;153:1641-1646.
- Campochiaro PA. Retinal and choroidal neovascularization. *J Cell Physiol*. 2000;184:301-310.
- Heckenlively JR, Hawes NL, Friedlander M, et al. Mouse model of subretinal neovascularization with choroidal anastomosis. *Retina*. 2003;23:518-522.
- Bischoff P, Flower R. Ten years experience with choroidal angiography using indocyanine green dye: a new routine examination or an epilogue? *Doc Ophthalmol*. 1985;60:235-291.
- Lopez-Saez MP, Ordoqui E, Tornero P, et al. Fluorescein-induced allergic reaction. *Ann Allergy Asthma Immunol*. 1998;81:428-430.
- Stanga PE, Lim JI, Hamilton P. Indocyanine green angiography in chorioretinal diseases: indications and interpretation: an evidence-based update. *Ophthalmology*. 2003;110:15-21.
- Shah SM, Tatlipinar S, Quinlan E, et al. Dynamic and quantitative analysis of choroidal neovascularization by fluorescein angiography. *Invest Ophthalmol Vis Sci*. 2006;47:5460-5468.
- Kotsolis AI, Killian FA, Ladas ID, Yannuzzi LA. Fluorescein angiography and optical coherence tomography concordance for choroidal neovascularisation in multifocal choroiditis. *Br J Ophthalmol*. 2010;94:1506-1508.
- Makita S, Hong Y, Yamanari M, Yatagai T, Yasuno Y. Optical coherence angiography. *Opt Express*. 2006;14:7821-7840.
- Fingler J, Schwartz D, Yang C, Fraser SE. Mobility and transverse flow visualization using phase variance contrast with spectral domain optical coherence tomography. *Opt Express*. 2007;15:12636-12653.
- Tao YK, Davis AM, Izatt JA. Single-pass volumetric bidirectional blood flow imaging spectral domain optical coherence tomography using a modified Hilbert transform. *Opt Express*. 2008;16:12350-12361.
- An L, Wang RK. In vivo volumetric imaging of vascular perfusion within human retina and choroids with optical micro-angiography. *Opt Express*. 2008;16:11438-11452.
- Mariampillai A, Standish BA, Moriyama EH, et al. Speckle variance detection of microvasculature using swept-source optical coherence tomography. *Opt Lett*. 2008;33:1530-1532.
- Vakoc BJ, Lanning RM, Tyrrell JA, et al. Three-dimensional microscopy of the tumor microenvironment in vivo using optical frequency domain imaging. *Nat Med*. 2009;15:1219-1223.
- Yu L, Chen Z. Doppler variance imaging for three-dimensional retina and choroid angiography. *J Biomed Opt*. 2010;15:016029-016024.
- Enfield J, Jonathan E, Leahy M. In vivo imaging of the microcirculation of the volar forearm using correlation mapping optical coherence tomography (cmOCT). *Biomed Opt Express*. 2011;2:1184-1193.
- Blatter C, Klein T, Grajciar B, et al. Ultrahigh-speed non-invasive widefield angiography. *J Biomed Opt*. 2012;17:0705051-0705053.
- Choi W, Mohler KJ, Potsaid B, et al. Choriocapillaris and choroidal microvasculature imaging with ultrahigh speed OCT angiography. *PLoS One*. 2013;8:e81499.
- Jia Y, Bailey ST, Wilson DJ, et al. Quantitative optical coherence tomography angiography of choroidal neovascularization in age-related macular degeneration. *Ophthalmology*. 2014;121:1435-1444.
- Moult E, Choi W, Waheed NK, et al. Ultrahigh-speed swept-source OCT angiography in exudative AMD. *Ophthalmic Surg Lasers Imaging Retina*. 2014;45:496-505.
- Choi W, Moult EM, Waheed NK, et al. Ultrahigh-speed, swept-source optical coherence tomography angiography in non-exudative age-related macular degeneration with geographic atrophy. *Ophthalmology*. 2015;122:2532-2544.
- Kim DY, Fingler J, Zawadzki RJ, et al. Noninvasive imaging of the foveal avascular zone with high-speed, phase-variance optical coherence tomography. *Invest Ophthalmol Vis Sci*. 2012;53:85-92.

32. Schwartz DM, Fingler J, Kim DY, et al. Phase-variance optical coherence tomography. *Ophthalmology*. 2014;121:180-187.
33. Jia Y, Wei E, Wang X, et al. Optical coherence tomography angiography of optic disc perfusion in glaucoma. *Ophthalmology*. 2014;121:1322-1332.
34. Zhi Z, Cepurna WO, Johnson EC, Morrison JC, Wang RK. Impact of intraocular pressure on changes of blood flow in the retina, choroid, and optic nerve head in rats investigated by optical microangiography. *Biomed Opt Express*. 2012;3:2220-2233.
35. Zhi Z, Chao JR, Wietecha T, Hudkins KL, Alpers CE, Wang RK. Noninvasive imaging of retinal morphology and microvasculature in obese mice using optical coherence tomography and optical microangiographyretinal OCT/OMAG in obese mice. *Invest Ophthalmol Vis Sci*. 2014;55:1024-1030.
36. Lee J, Jiang JY, Wu W, Lesage F, Boas DA. Statistical intensity variation analysis for rapid volumetric imaging of capillary network flux. *Biomed Opt Express*. 2014;5:1160-1172.
37. Schneider CA, Rasband WS, Eliceiri KW. NIH Image to ImageJ: 25 years of image analysis. *Nat Meth*. 2012;9:671-675.
38. Cho HS, Jang S-J, Kim K, et al. High frame-rate intravascular optical frequency-domain imaging in vivo. *Biomed Opt Express*. 2014;5:223-232.
39. Jun C, Villiger M, Oh W-Y, Bouma BE. All-fiber wavelength swept ring laser based on Fabry-Perot filter for optical frequency domain imaging. *Opt Express*. 2014;22:25805-25814.
40. Yun SH, Tearney GJ, de Boer JF, Bouma BE. Removing the depth-degeneracy in optical frequency domain imaging with frequency shifting. *Opt Express*. 2004;12:4822-4828.
41. Fukuchi T, Takahashi K, Shou K. Optical coherence tomography (OCT) findings in normal retina and laser-induced choroidal neovascularization in rats. *Graefes Arch Clin Exp Ophthalmol*. 2001;39:41-46.
42. Giani A, Thanos A, Roh MI, et al. In vivo evaluation of laser-induced choroidal neovascularization using spectral-domain optical coherence tomography. *Invest Ophthalmol Vis Sci*. 2011;52:3880-3887.
43. Berger A, Cavallero S, Dominguez E, et al. Spectral-domain optical coherence tomography of the rodent eye: highlighting layers of the outer retina using signal averaging and comparison with histology. *PLoS One*. 2014;9:e96494.